Sexual Dimorphism Is Associated With Corneal Nerve and Epithelial Alterations and Tear-Film Defects in Pax6 Haploinsufficiency Mouse Model

Marjolaine Willems,[1–3] Mélissa Girard,[1] Nadège Feret,[1] Dylan Touchet,[1] Jérôme Vialaret,[1,4] Jana Kindermans,[1,4] Laura Fichter,[1,4] Christophe Hirtz,[1,4] Dominique Bremond-Gignac,[5] Vincent Daien,[1,3,6,7] Cécile Delettre,[1] Marie Pequignot,[1] and Frederic Michon[1,6]

[1]Institute for Neurosciences of Montpellier, University of Montpellier, INSERM, Montpellier, France
[2]Department of Clinical Genetics, Arnaud de Villeneuve Hospital, University Hospital of Montpellier, Montpellier, France
[3]OPHTARA Rare Disease Competence Center, University Hospital of Montpellier, Montpellier, France
[4]IRMB-PPC, University of Montpellier, University Hospital of Montpellier, INSERM CNRS, Montpellier, France
[5]Department of Ophthalmology, University Hospital Necker Enfants Malades, APHP, Paris, INSERM UMRS 1138, T17, Centre de Reference Maladies Rares OPHTARA Rare Disease Reference Center, Paris, France
[6]Department of Ophthalmology, Gui de Chauliac Hospital, University Hospital of Montpellier, Montpellier, France
[7]The Save Sight Institute, Sydney Medical School, The University of Sydney, Sydney, New South Wales, Australia

Correspondence: Frederic Michon, Institute for Neurosciences of Montpellier, University of Montpellier, INSERM, 80 Avenue Augustin Fliche – BP 74103, Montpellier cedex 5 34091, France; frederic.michon@inserm.fr.

Received: November 19, 2025
Accepted: April 23, 2026
Published: May 18, 2026

Citation: Willems M, Girard M, Feret N, et al. Sexual dimorphism is associated with corneal nerve and epithelial alterations and tear-film defects in Pax6 haploinsufficiency mouse model. *Invest Ophthalmol Vis Sci.* 2026;67(5):39. https://doi.org/10.1167/iovs.67.5.39

Purpose. The purpose of this study was to determine how *Pax6* haploinsufficiency alters epithelial maturation, immune balance, sensory innervation, and lacrimal function across the ocular surface, and how these defects affect corneal repair.

Methods. *Pax6*^{tm1Ued} mice crossed with CMV-Cre were used to generate *Pax6*$^{+/-}$ animals. Ocular-surface maturation, epithelial organization, immune infiltration, and sensory innervation were assessed by whole-cornea immunostaining. Standardized corneal abrasion was used to evaluate epithelial and neural repair. Corneal RNA sequencing and tear-film proteomics were performed in both sexes to define genotype- and sex-dependent molecular programs.

Results. *Pax6*$^{+/-}$ mice showed heterogeneous ocular phenotypes, delayed eyelid opening, reduced KRT12, persistent central KRT14 expansion, and a sustained deficit in central proliferation. Immune infiltration was elevated from eyelid opening onward. Corneal nerves were markedly reduced and disorganized, with decreased sensitivity despite minimal trigeminal transcriptional changes. Transcriptomics revealed sex-specific gene-expression patterns converging on inflammation and extracellular-matrix remodeling. After abrasion, closure rates were preserved, but *Pax6*$^{+/-}$ corneas failed to fully restore normal epithelial identity, territorial patterning, or nerve density. Tear secretion was impaired in a sex-dependent manner, and proteomics showed depletion of structural and antioxidant proteins with exaggerated inflammatory and keratinization responses after injury.

Conclusions. Our model showed that *Pax6* haploinsufficiency is associated with epithelial dysmaturation, chronic inflammation, denervation, defective repair, and sex-modulated lacrimal dysfunction. These integrated abnormalities mirror key features of AAK and underline inflammation, neurotrophic support, and tear-film quality as therapeutic targets.

Keywords: PAX6, aniridia-associated keratopathy (AAK), wound healing, sexual dimorphism

Congenital aniridia is a rare autosomal dominant disorder most commonly caused by pathogenic variants in the transcription factor PAX6 and is characterized by marked clinical heterogeneity.[1] In addition to the hallmark iris hypoplasia, patients frequently present with a broad spectrum of ocular abnormalities involving the retina, optic nerve, iridocorneal angle, and lens, together with nystagmus, cataract, glaucoma, progressive keratopathy, and severe visual impairment.[2] Among these manifestations, aniridia-associated keratopathy (AAK) is particularly debilitating. This progressive, vision-threatening disease is characterized by recurrent epithelial breakdown, stromal remodeling, and scarring, ultimately leading to corneal opacification and, if left untreated, blindness.[3–5] Although AAK is often linked to limbal stem cell dysfunction, it also encompasses more widespread alterations of the ocular surface.

Understanding the development and progression of AAK requires an integrated view of corneal biology. The cornea

is an avascular, transparent tissue that both refracts light and protects the eye from injury and infection.[6,7] Its outer epithelium is in direct contact with the tear film, the collagen-rich stroma provides mechanical strength, and the endothelial monolayer maintains deturgescence. Epithelial integrity depends on basal cells and limbal epithelial stem cells (LESCs) located at the corneal periphery, whereas apical microvilli contribute to tear-film distribution and host defense.[8,9] The ocular surface also comprises an active immune network connected to vascular and lymphatic systems which, when dysregulated, can exacerbate local inflammation and tissue pathology.[10–12] Equally important is the dense sensory innervation of the cornea: peripheral afferents form subepithelial and subbasal plexuses that regulate epithelial migration, wound healing, and inflammatory crosstalk.[13,14]

The tear film overlies this tissue architecture and is essential for lubrication, epithelial nourishment, and antimicrobial defense. Proteins secreted predominantly by the lacrimal glands support epithelial homeostasis and immune surveillance, and advances in tear proteomics have identified biomarkers associated with both ocular and systemic disease.[15–17] Because AAK involves defects in epithelial renewal, innervation, inflammation, and tear composition,[18,19] an integrated analysis across these different levels is required to distinguish the primary consequences of PAX6 insufficiency from secondary, and potentially modifiable, changes.

Mouse models have been instrumental in providing mechanistic insight, as the murine eye reproduces key features of human ocular biology despite lacking a cone-rich macula.[20,21] Importantly, the PAX6 coding sequence is conserved between mouse and human, supporting the translational relevance of these models.[22] Previous Pax6 mutant models recapitulate corneal abnormalities and lacrimal gland hypoplasia.[22,23] At the molecular level, *Pax6$^{Sey/+}$* corneas display features of a chronic wound state, including junctional instability, cytoskeletal remodeling, and activation of stress-related pathways, even in the absence of injury.[24,25] Functionally, *Pax6$^{+/-}$* epithelium exhibits delayed wound closure associated with impaired early ERK1/2 activation and altered calcium signaling, although dysregulated apoptosis may further compromise repair.[26,27] Taken together, these findings suggest that Pax6 haploinsufficiency impairs acute epithelial responses and renders the cornea susceptible to cumulative damage induced by otherwise minor insults.

Here, we extend this body of work by investigating corneal homeostasis and repair in a conditional *Pax6^{tm1Ued}* model in which the exons encoding the paired DNA-binding domain are flanked by loxP sites.[28] By crossing this line with CMV-Cre to generate heterozygous Pax6$^{+/-}$ mice, we assessed the systemic consequences of Pax6 haploinsufficiency across the ocular surface. We focused primarily on epithelial differentiation, immune activation, sensory innervation, and repair dynamics, and integrated corneal transcriptomics with tear proteomics to provide complementary mechanistic insight into ocular surface homeostasis under baseline conditions and following standardized corneal abrasion.

Our results reveal coordinated defects in tissue architecture, innervation, and wound healing, accompanied by both quantitative and qualitative alterations in the tear film. These findings define mechanistic links between Pax6 dosage and the multilayered physiology of the ocular surface, provide a framework for understanding AAK progression, and identify candidate points of intervention that may be therapeutically exploitable.

Materials and Methods

Animals Used in This Study

The Pax6^{tm1Ued} allele was created by inserting a neo cassette, bordered by 2 loxP sites, into intron 4 of the *Pax6* gene (in the same orientation as the endogenous locus), with an additional loxP site placed in intron 6. This configuration means that exons 5, 5a, and 6, which are responsible for the paired domain, are flanked by loxP sites. When the conditional null *Pax6^{fl}* allele is exposed to Cre-recombinase, recombination occurs at the loxP sites, leading to the deletion of exons 5, 5a, and 6, which are essential for PAX6 function. This deletion is anticipated to result in a nonsense frame-shift mutation, transforming the floxed *Pax6^{fl}* allele into the deleted *Pax6*Δ variant, effectively rendering it a null allele.[28]

The floxed Pax6^{tm1Ued} mouse line (Riken) was used to generate heterozygous CMV-Cre$^{+/-}$ *Pax6$^{tm1Ued/+}$* mice (hereafter referred to as *Pax6$^{+/-}$*), which were compared to their littermate CMV-Cre$^{-/-}$ *Pax6$^{tm1Ued/+}$* mice (*Pax6$^{+/+}$*) used as controls. Heterozygous *Pax6$^{+/-}$* and *Pax6$^{+/+}$* mice were obtained by crossing *Pax6$^{tm1Ued/tm1Ued}$* mice with inbred CMV-Cre$^{+/-}$ Swiss mice and were genotyped by polymerase chain reaction (PCR). Mice harboring *Pax6WT*, *Pax6^{tm1Ued}*, and Pax6^{del} alleles were genotyped using PCR manufacturer protocol (https://mus.list.brc.riken.jp/ja/wp-content/pdf/05945_PCR.pdf). Cre recombinase-expressing transgenic mice were genotyped using primers to the Cre cassette forward: 5'-GCG GTC TGG CAG TAA AAA CTA TC and reverse: GTG AAA CAG CAT TGC TGT CAC TT.

The mice were kept under a 12-hour light/dark cycle with free access to food and water. The animals were euthanized by cervical dislocation. All experimental procedures were approved by the local ethics committee and the Ministry of Research and Higher Education (authorization 2016,080,510,211,993 version 2). All procedures were carried out in compliance with French regulations on animal experimentation (French decree 2013-118) and the specific European Union guidelines on animal welfare (Directive 2010/63/EU). The study adheres to the ARRIVE guidelines and the ARVO Statement for the Use of Animals in Ophthalmic and Vision Research.

Monitoring Corneal Abrasions and Healing Process

Corneal abrasion was conducted as previously described.[29,30] The epithelium was abraded unilaterally on the right eye with an ocular burr (Algerbrush II, reference BR2–5 0.5 mm, The Alger Company, USA) on mice anesthetized with ketamine (90 mg/kg, Imalgene 1000) and xylazine (10 mg/kg, Rompun) administered intraperitoneally. The abraded area was examined with fluorescein solution (1% in PBS, Sigma-Aldrich) under blue cobalt light. Following the procedure, Ocrygel was applied to the eyes, and mice received buprenorphine (0.1 mg/kg, Buprecare) via intraperitoneal injection. The healing process of the abrasion was monitored daily using fluorescein solution on restrained mice, and images were captured with a camera.

Investigative Ophthalmology & Visual Science

Table 1. Primary Antibodies Used for Cornea Immunostaining

Antibody Name	Host	Vendor/Reference	Dilution
Purified anti-keratin 14 antibody	Chicken	BioLegend/906004	1:500
Cytokeratin 12 recombinant rabbit monoclonal antibody (2M1K10)	Rabbit	Invitrogen/MA5-42701	1:200
Anti-CD45 antibody [IBL-3/16]	Rat	Abcam/ab23910	1:200
Anti-PAX6 antibody [EPR3352(2)]	Rabbit	Abcam/ab1092233	1:500
Anti-Histone H3 (phospho S28) antibody [HTA28]	Rat	Abcam/10543	1:500
Anti-beta III tubulin antibody - neuronal marker	Rabbit	Abcam/ab18207	1:1000
Anti-TRPM8	Rabbit	Alomone Labs	1:500

Table 2. Secondary Antibodies Used for Cornea Immunostaining

Antibody Name	Host	Target	Vendor/Reference	Dilution
Goat anti-rabbit IgG (H+L) cross-adsorbed Secondary antibody, Alexa Fluor 488	Goat	Rabbit	ThermoFisher Scientific/A-11008	1:500
Goat Anti-Chicken IgY H&L (Alexa Fluor 568) preadsorbed	Goat	Chicken	Abcam/ab175711	1:500
Goat anti-rat IgG H&L (Alexa Fluor 647) preadsorbed	Goat	Rat	Abcam/ab150167	1:500
Goat anti-rat IgG H&L (Alexa Fluor 568)	Goat	Rat	Abcam/ab175476	1:500

Assessment of Sensitivity

Sensitivity was assessed using Von Frey filaments (Bioseb, France, reference bio-VF-M), as previously described.[31] The filaments exert a force ranging from 0.008 to 0.6*g* when applied to the center of the cornea of an immobilized mouse. The force is increased by selecting different filaments until an eye-blink reflex is elicited. The Von Frey test was conducted over 3 consecutive days, and the results for each cornea were averaged. Sensitivity was expressed as the inverse of the von Frey filament force required to elicit a blink reflex (g^{-1}), so that higher values indicate greater corneal sensitivity. All experiments were performed by the same experimenter.

Tissue Collection and Processing

For immunostaining purposes, following mice euthanasia by cervical dislocation, the eyes were enucleated by severing the optic nerve and fixed in a 4% paraformaldehyde solution (Antigenfix, Diapath, reference P0014) for 20 minutes. After washing with PBS, the eyes were dehydrated for 2 hours in a 50% ethanol/PBS solution before being stored in 70% ethanol/PBS at 4°C.

For transcriptomic analysis, following mice euthanasia by cervical dislocation, the eyes were enucleated by severing the optic nerve. After direct dissection, each cornea was frozen in a tube immediately immersed in liquid nitrogen before being stored at −80°C. Trigeminal ganglia were collected and placed in lysis solution, snap frozen, and then stored at −80°C.

Whole Corneas Immunostaining

For immunostaining analyses, the unit of analysis was the animal. When both eyes from a given animal were collected, they were assigned to different stainings rather than used for the same experimental dataset, in order to ensure biological independence while minimizing animal use in accordance with ARRIVE guidelines. The eyes were rehydrated for 2 hours in a solution of 50% ethanol/PBS at room temperature. After two 10-minute incubations in PBS, the corneas were dissected and subsequently blocked and permeabilized in a solution of 5% FSG (Sigma-Aldrich, reference G7765) and 5% goat serum (GS) (Thermo Fisher Scientific, reference 16,210,064) in 0.5% PBS/Triton X-100 at room temperature. The corneas were then incubated overnight at 4°C with primary (Table 1) and secondary antibodies (Table 2) in a solution of 5% FSG and 5% GS in 0.1% PBS/Triton X-100, followed by 3 rinses of 1 hour each in 0.1% PBS/Triton X-100. Nuclei were stained using Hoechst 33342 (Thermo Fisher Scientific, reference H3570) for 10 minutes and rinsed in PBS.

Four incisions were made on all corneas, which were then mounted in Vectashield medium (Vector Laboratories, H-1000), with the endothelium facing the slide.

Image Acquisition and Processing

Image acquisition was conducted as previously described.[31] Whole-cornea images were captured using a Leica Thunder Imager Tissue microscope with the navigator module and the large volume computational clearing (LVCC) process. Images were obtained with LAS X software (version 3.7.4) using a 20X/0.55 objective and were subsequently processed with Imaris Bitplane software (version 9.8.0). Consistent parameters were used for the acquisition and processing of all images within a single panel.

Statistical Analysis

Data were analyzed using GraphPad Prism (version 10.2.2). Multiple unpaired two-tailed Student's *t*-tests were performed, with false discovery rate (FDR) control using the two-stage Benjamini, Krieger, and Yekutieli procedure. Exact adjusted *P* values are reported, together with mean ± SEM. On figures, each data point represents an individual biological replicate. Statistical significance is indicated directly on the figures for each comparison.

Because distinct analytical pipelines were used for proteomic and transcriptomic experiments, the detailed statistical frameworks, including normalization, differential analysis, and FDR control, are provided in the dedicated Methods sections.

Investigative Ophthalmology & Visual Science

Transcriptomic Analysis

RNA Isolation and cDNA Library Preparation. Frozen corneas and trigeminal ganglia were shipped on dry ice to Beijing Genomics Institute (BGI; Shenzhen, China) for library construction and sequencing on the DNBseq platform. Total RNA was extracted using the RNeasy Mini Kit (Qiagen). Polyadenylated RNA was captured with oligo(dT)-coupled magnetic beads and fragmented. RNA integrity and fragment-size distributions were assessed on a Fragment Analyzer; only samples meeting predefined quality control (QC) thresholds advanced to library preparation. Libraries were generated with the BGI Optimal Dual-mode mRNA Library Prep Kit and sequenced on a DNBSEQ-T7 (paired-end 2 × 100 bp; approximately 50 million clean reads per sample). Adapters, contaminants, and low-quality bases/reads were removed with SOAPnuke.[32] Filtered reads were aligned to the mouse reference genome (Mus_musculus_10090; UCSC mm10 v2201) with HISAT2, and gene-level counts were obtained using HTSeq-count to produce the raw count matrix.

Transcriptomic Data Analysis. Primary analyses were performed with BGI's Dr. Tom multi-omics platform (https://biosys.bgi.com). Briefly, clean reads were also aligned against the gene set (including known/novel, coding/non-coding transcripts) using Bowtie2,[33] and transcript/gene abundance was estimated with RSEM version 1.3.1 (Li and Dewey, 2011). Heatmaps were generated with pheatmap version 1.0.12 based on relative expression across samples. Differential expression was assessed with DESeq2 version 1.34.0,[34] applying FDR correction and reporting q values (significant at $q \leq 0.05$; in stringent analyses FDR ≤ 0.001). Functional enrichment for Gene Ontology (GO; (www.geneontology.org), Kyoto Encyclopedia of Genes and Genomes (KEGG; www.kegg.jp), and Reactome (https://reactome.org) terms were evaluated with a hypergeometric test (Phyper), with multiple-testing correction by q value and significance set at $q \leq 0.05$.

Tear Collection and Quantitative Evaluation

Tear samples were sequentially collected from each eye for one minute using 1 µL microcapillary glass tubes (Merck, Drummond Scientific, reference P1424-1PAK) and volumes were evaluated by comparing the relative distance covered in 1 minute within the collection capillary between *Pax6*$^{+/+}$ and *Pax6*$^{+/-}$ mice.

Proteomic Analysis: Sample Collection and Pooling. For comparisons (right eye), due to the limited tear volume obtained per eye following corneal abrasion, tears from the right eye of two mice matched for sex, genotype, and condition were pooled to obtain sufficient protein yield for liquid-chromatography tandem mass spectrometry (LC-MS/MS) analysis. Each pooled sample constituted one biological replicate. No animal contributed to more than one pool. Tears were then brought to 12 µL with ammonium bicarbonate (ABC) buffer. Samples were maintained on ice during collection (4°C) and stored at −80°C until processing.

Protein Quantification and Solution-Phase Digestion. Frozen tear samples were thawed on ice (4°C). Total protein was quantified on a NanoDrop One UV–Vis spectrophotometer (Thermo Fisher Scientific, ND-ONE-W) using 2 µL per sample. Aliquots containing 5 µg total protein were reduced, alkylated, and digested with trypsin via the automated SP3 workflow on a Bravo 96LT platform (Agilent Technologies). Resulting peptides were desalted and injected in technical triplicate for LC-MS/MS on an Evosep One coupled to a timsTOF HT (Bruker Daltonics).

LC-MS/MS Acquisition. For Q-TOF analyses, peptides were reconstituted in 10 µL phase A (2% acetonitrile and 0.1% formic acid in HPLC-grade water) and transferred to polypropylene MS vials (Agilent, 5190-3155). One-microliter injections were analyzed in triplicate on a NanoElute HPLC (Bruker) coupled to an Impact II quadrupole time-of-flight mass spectrometer (Bruker). Separations used a C18 column (FORTY, Bruker, 75 µm × 400 mm; 1.9 µm, 120 Å) with the following gradient: 2% to 15% B over 55 minutes, 15% to 25% B over 25 minutes, 25% to 35% B over 10 minutes, and 35% to 95% B over 10 minutes (phase A: 2% ACN/0.1% FA and phase B: 90% ACN/0.1% FA). Column temperature was 50°C and flow rate 300 nL/min. All solvents (water, ACN, and FA) were HPLC grade (Biosolve, Dieuze, France).

Data Processing and Statistics. Protein identification was performed with DIA-NN version 1.8.1 using trypsin specificity (≤1 missed cleavage), minimum peptide length of 7 aa, precursor charge 1 to 4, precursor m/z 300 to 1800, and 1% protein-level FDR. Searches referenced the UniProt Mus musculus proteome (Release_2024_03). Variable modifications included Asn deamidation and Met oxidation; Cys carbamidomethylation was set as fixed, with a maximum of two variable modifications per peptide.

Label-free quantification (LFQ) intensities were processed in DIA-Analyst version 0.8.6. For biological replicates, proteins lacking ≥70% valid values in at least one group were excluded. LFQ values were log2-transformed and grouped by genotype. Missing values were imputed using the bpca method. Differential abundance was assessed with t-statistics, applying an adjusted P value cutoff of 0.05 to define significantly regulated proteins. Volcano plots denote proteins increased in red and decreased in blue for each comparison.

Functional enrichment of significantly modulated proteins was performed with Enrichr (https://maayanlab.cloud/Enrichr/) using GO Biological Process 2025 and Reactome Pathways 2024 annotations.

Availability of Data and Materials

The raw data are available upon request to the corresponding author and the datasets produced for the current study are publicly available. The RNA-sequencing (RNA-seq) data is available in the GEO repository, under the accession numbers GSE326648. The MS proteomics data are available in the PRIDE repository, via ProteomeXchange, with the identifier PXD070553.

Results

Variable Ocular Phenotype and Delayed Eyelid Opening in *Pax6*$^{+/-}$ Mice

To evaluate the phenotype of our mouse of interest, we investigated the ocular structures in the different mouse lines. The parental mice: CMV-Cre$^{+/-}$, *Pax6*$^{+/+}$ mice, CMV-Cre*Pax6*$^{tm1Ued/\,tm1Ued}$ mice and the littermates *CMV-Cre*$^{-/-}$ *Pax6*$^{tm1Ued/+}$ (named *Pax6*$^{+/+}$) mice did not exhibit any detectable phenotype, particularly at the ocular level, whereas CMV-Cre$^{+/-}$, Pax6$^{+/tm1Ued}$ (named *Pax6*$^{+/-}$)

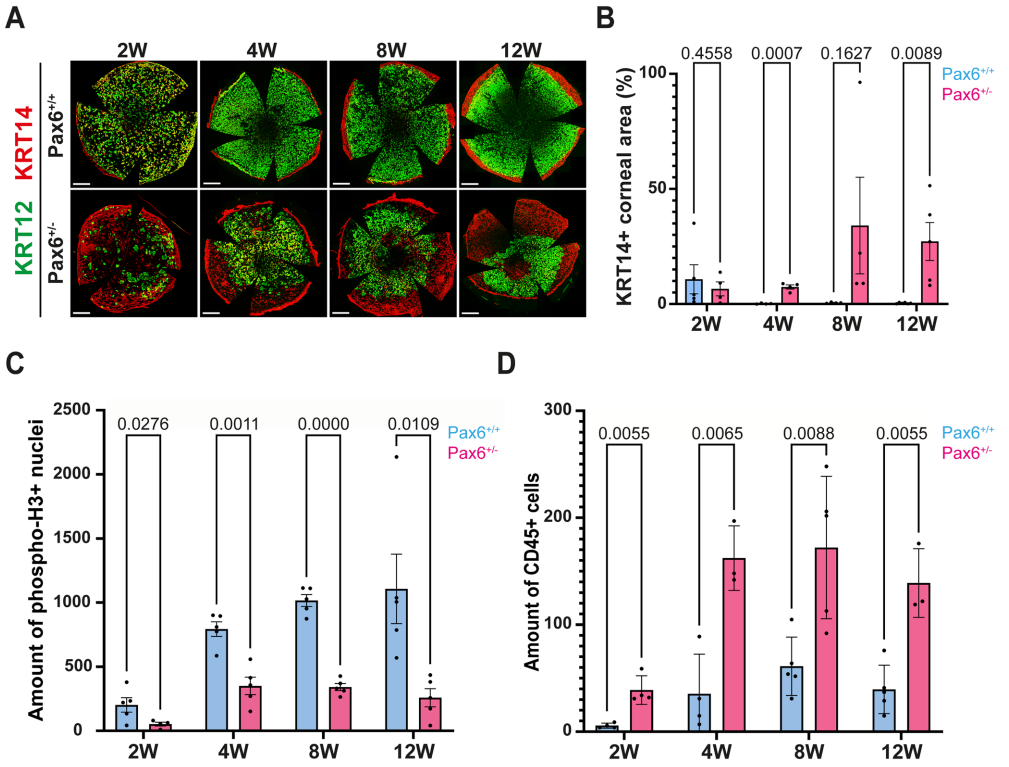

Figure 1. Early and persistent corneal differentiation abnormality in mutants revealed by KRT12/KRT14 staining. (**A**) The visualization of KRT12/KRT14 staining on whole corneas shows defective corneal regionalization in mutants from postnatal week 2 to 12 (*Scale bars* = 500 µm). (**B**) Quantification of KRT14 across the same stages, reporting the percentage of total corneal area covered by KRT14 staining, measured with Imaris (n = 4–6 different animals per group). (**C**) Early and persistent defect in central proliferation in mutants, demonstrated by quantifying the number of nuclei expressing phospho-Histone 3 (pH3). After marking pH3 by immunohistochemistry on whole corneas, the number of nuclei expressing pH3 in the central area covering 50% of the whole corneal surface is then measured for each stage using Imaris software. As soon as 24 weeks, mutants show significant defective proliferation (n = 5 different animals per group). (**D**) Early and persistent corneal inflammation in *Pax6*$^{+/-}$ mutants. CD45 immunolabeling (pan-leukocyte marker) was quantified at each stage. At 2 weeks, *Pax6*$^{+/-}$ corneas already showed significantly elevated infiltration compared to *Pax6*$^{+/+}$ (x4.7). This difference remained high at 3 months of age (n = 3–5 different animals per group). Each data point represents one animal (biological replicate). Data are represented as mean ± SEM; statistical analysis was performed using multiple unpaired two-tailed Student's t-tests with false discovery rate control (2-stage Benjamini, Krieger, and Yekutieli procedure). Statistical significance is indicated directly on the figures. Time notation: W = weeks.

mice consistently displayed ocular abnormalities with variable and sometimes asymmetric expressivity, including microphthalmia, corneal opacity, iris hypoplasia/aniridia, and cataract, indicating variable penetrance of individual features, as seen in patients.

To obtain an early, quantitative readout of postnatal maturation, we assessed the timing of eyelid opening, a well-established developmental milestone for the ocular surface maturation.[35] *Pax6*$^{+/-}$ pups exhibited delayed eyelid opening compared with *Pax6*$^{+/+}$ littermates. At postnatal day 15 (P15), 37.5% of *Pax6*$^{+/-}$ mice (3/8) had not yet opened their eyelids, whereas all *Pax6*$^{+/+}$ littermates (11/11) had completed eyelid opening ($P < 0.05$), supporting a genotype-dependent delay in postnatal ocular surface maturation (data not shown).

Functionally, the postponed eyelid opening points to impaired coordination of epithelial maturation, tear film establishment, and periocular morphogenesis, processes known to depend on adequate *PAX6* dosage. These observations provide an in vivo correlate of the clinical heterogeneity seen in human aniridia and establish a developmental context for subsequent analyses of corneal structure, innervation, and epithelial homeostasis.

Pax6 Haploinsufficiency Disrupts Corneal Maturation and Homeostasis

To assess epithelial differentiation, we profiled KRT12 (terminal corneal marker) and KRT14 (basal/progenitor marker). In *Pax6*$^{+/+}$ mice, the immature cornea at 2 weeks showed widespread KRT12/KRT14 co-expression; from 4 week onward, a stable adult pattern emerged with KRT12 across the full cornea and KRT14 confined to basal limbal/peripheral cells. In *Pax6*$^{+/-}$ mice, KRT12 was markedly reduced at 2 weeks and KRT14 extended centrally. KRT12 partially recovered between 4 and 8 weeks but never reached wild-type coverage; by 12 weeks, KRT12 was restricted to small central islands whereas KRT14 progressively invaded paracentral and central regions (Figs. 1A, 1B). These data indicate a persistent differentiation defect, with an abnormal centripetal expansion of undifferentiated basal-like cells evident from eyelid opening and persisting at 3 months of age.

Given prior reports of altered turnover in *Pax6* mutants, we quantified mitoses using phospho-histone H3 within the central 50% of the cornea to minimize limbal contributions. *Pax6*$^{+/-}$ corneas showed an early and sustained reduc-

Investigative Ophthalmology & Visual Science

tion in mitotic figures at 4 weeks (−55% vs *Pax6*$^{+/+}$) that persisted at 8 weeks and 12 weeks, whereas *Pax6*$^{+/+}$ corneas displayed uniformly low central proliferation across ages (Fig. 1C). Together, PAX6 deficiency compromises epithelial maturation and central homeostasis.

Early and Sustained Immune Infiltration

Building on reports that immune activation emerges early in human AAK, we quantified leukocyte infiltration in the cornea using the pan-leukocyte antigen CD45 as a readout of inflammatory burden. Immunolabeling and image-based cell counts revealed a robust increase in CD45+ cells in Pax6$^{+/-}$ corneas as early as 2 weeks postnatal, that is, at the developmental window that coincides with eyelid opening. At this stage, *Pax6*$^{+/-}$ corneas contained 4.7-fold more CD45+ cells than *Pax6*$^{+/+}$ controls, indicating that immune recruitment is already underway at the onset of ocular surface exposure.

This heightened leukocyte presence was not transient. Elevated CD45+ cell density persisted at 3 months of age, demonstrating that inflammatory tone remains chronically increased under PAX6 haploinsufficiency (Fig. 1D).

Pronounced Sensory Innervation Defects and Reduced Corneal Sensitivity

We next quantified corneal nerves using β3-tubulin and examined a specific sensory subset (TRPM8+ cold-sensitive C-fiber terminals). In 3-month-old *Pax6*$^{+/+}$ corneas, a dense, orderly network radiated from the periphery to a well-defined central vortex. *Pax6*$^{+/-}$ corneas exhibited a striking loss and disorganization of fine fibers, with an approximately 50% reduction in small-fiber density by volumetry, and attenuated TRPM8 trajectories (Fig. 2). Consistent with these architectural defects, epicritic sensitivity was significantly reduced in *Pax6*$^{+/-}$ mice.

Because corneal sensory fibers arise from trigeminal ganglion (TG) neurons, we profiled TG transcripts. Despite known sex differences at the ocular surface, differential expression in the TG was minimal (16 RNAs in male and 5 in female mice; 2 shared; Supplementary Table S1).

Corneal Transcriptomics Reveal Sex-Dependent Consequences of *Pax6* Haploinsufficiency

To disentangle epithelial fragility, inflammation, innervation defects, we performed sex-stratified corneal RNA-seq (Supplementary Table S2).

In *Pax6*$^{+/+}$ corneas, pathway-level sex differences were modest (Fig. 3). Male-higher transcripts modestly enriched cell-cycle/mitotic terms, whereas female-higher transcripts weakly enriched polyamine metabolism; KEGG did not yield significant pathways ($q < 0.05$; Supplementary Fig. S1).

By contrast, *Pax6*$^{+/-}$ corneas displayed a marked sex-dependent split. Female-higher transcripts enriched ribosome biogenesis, mRNA splicing/processing, and translational control; male-higher transcripts mapped to transmembrane/ion transport, vitamin/cofactor handling, N-glycan biosynthesis, and circadian programs (Supplementary Fig. S2). Venn analysis showed extensive sex-specific gene sets (2164 female-unique, 2110 male-unique, and 2732 shared), yet both sexes converged on common biological themes: inflammation and extracellular-matrix (ECM) remodeling (Supplementary Figs. S3, S4). KEGG highlighted cytokine–receptor interaction, leukocyte transendothelial migration, focal adhesion, PI3K–Akt, and Rap1 signaling. Reactome/GO pointed to ECM organization, hemostasis/platelet activation, innate immunity, cell adhesion, angiogenesis, and ERK1/2 activation.

Sex-specific modules diverged around this shared core. Female mice showed selective downregulation of metabolic programs (e.g., xenobiotic/drug metabolism via cytochrome P450, glutathione metabolism, retinol metabolism, and reduced transmembrane transport). Male mice showed heightened innate immunity (neutrophil degranulation, antigen cross-presentation, and complement) and repression of visual/phototransduction pathways. Thus, *Pax6* haploinsufficiency elicits a shared inflammatory/ECM program modulated by female-biased metabolic suppression versus male-biased sensory repression with amplified innate responses.

Wound Healing Uncovers Structural and Neural Repair Deficits

Macroscopic fluorescein assays revealed no genotype difference in overall epithelial closure time, indicating preserved resurfacing. We therefore assessed epithelial identity, tissue organization, and neural recovery at the microscopic level after abrasion.

PAX6 staining was comparable at baseline across genotypes. Two days post-abrasion, *Pax6*$^{+/+}$ corneas regained the characteristic patchy/intense PAX6 pattern, whereas *Pax6*$^{+/-}$ corneas showed a uniform but markedly reduced signal. This divergence persisted at 3 weeks post-abrasion, with *Pax6*$^{+/-}$ corneas failing to recover the pre-injury pattern (Fig. 4A).

KRT14 regionalization similarly diverged. At 2 days, both genotypes displayed paracentral/peripheral KRT14 consistent with mobilization of undifferentiated basal cells. By 3 weeks, KRT14 had re-restricted to the periphery in *Pax6*$^{+/+}$ corneas, whereas *Pax6*$^{+/-}$ corneas retained diffuse KRT14 extending centrally; this abnormal pattern persisted at 7 weeks, indicating a failure to re-establish normal territorial organization (Fig. 4B).

Proliferation showed an initial transient parity post-injury, but by 3 weeks the pre-existing approximately 50% proliferation deficit in *Pax6*$^{+/-}$ central epithelium was again apparent (Fig. 4C).

Innervation recovery was slow overall: *Pax6*$^{+/+}$ corneas reached approximately 50% of baseline fiber density at 3 weeks post-abrasion and approached baseline by 7 weeks. Both genotypes recapitulated their pre-abrasion patterns by 3 weeks; however, the absolute difference between *Pax6*$^{+/+}$ and *Pax6*$^{+/-}$ nerves persisted through 7 weeks (Fig. 5) indicating incomplete neural restoration despite epithelial resurfacing. Sensory recovery lagged architecture: in *Pax6*$^{+/+}$ mice, epicritic sensitivity +remained at approximately 50% of baseline at 7-weeks post-abrasion. A significant sensitivity gap between genotypes was already evident by 4 weeks and remained thereafter.

Sex-Stratified Lacrimal Phenotypes and Tear-Film Proteome Remodeling

Given the tear film's roles in epithelial integrity, immune regulation, and neurotrophic support, we quantified tear secretion and profiled the tear proteome in *Pax6*$^{+/+}$ and *Pax6*$^{+/-}$ mice. Tear volume was reduced in *Pax6*$^{+/-}$ animals, and reached near-significance after sex stratification only

Investigative Ophthalmology & Visual Science

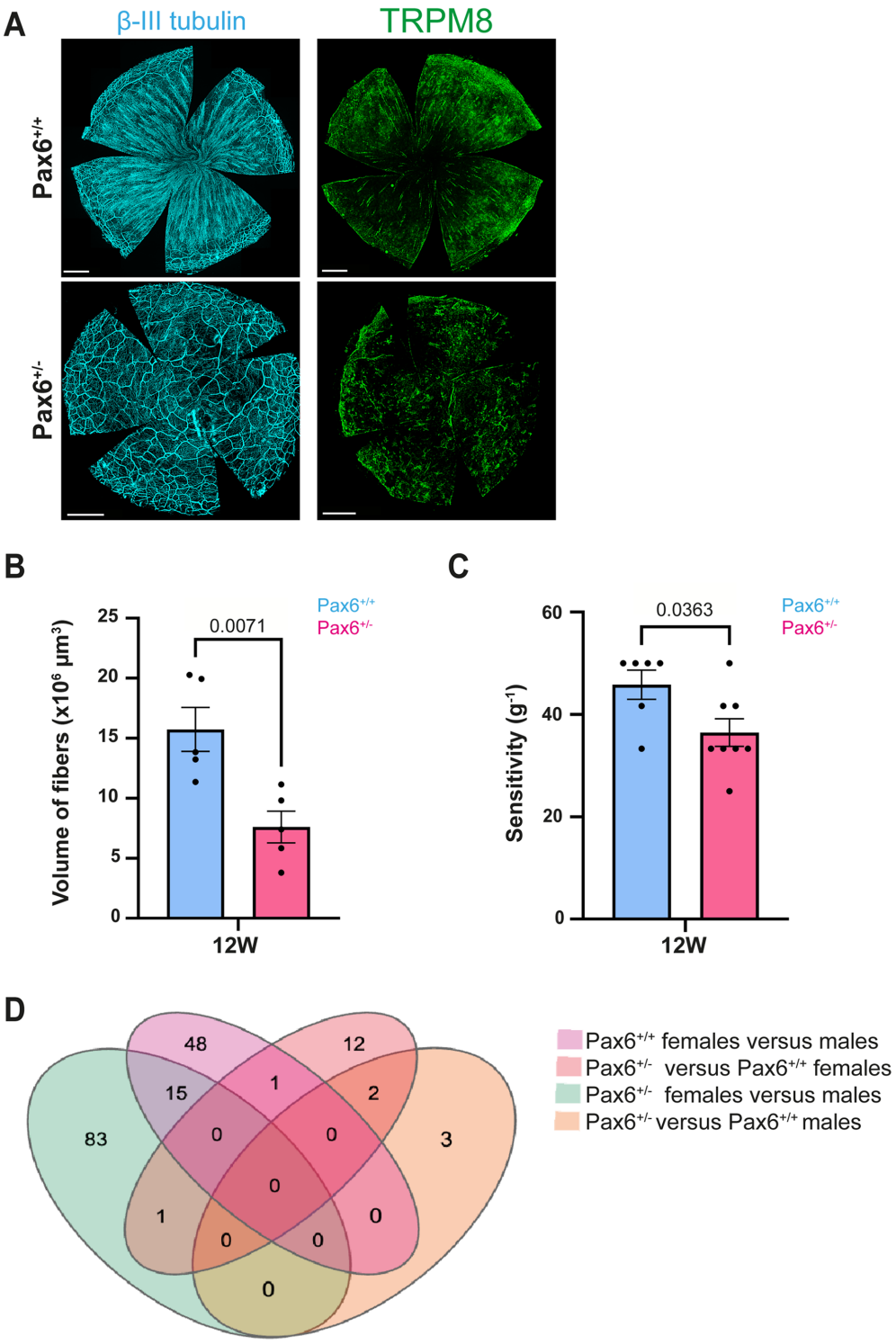

Figure 2. Defective corneal innervation, reduced mechanical sensitivity, and trigeminal ganglion transcriptomic differences in 3-month-old Pax6$^{+/-}$ mice. (**A**) Visualization and volume analysis of corneal innervation with β3-tubulin, and TRPM8. β3-tubulin immunostaining revealed a dense and well-organized corneal nerve architecture in *Pax6*$^{+/+}$ mice, with fine fibers radiating from the periphery and converging into a distinct central vortex, whereas *Pax6*$^{+/-}$ corneas showed a marked reduction and disorganization of fibers. TRPM8 staining, which labels cold-sensitive C-fiber terminals, displayed thin, radially oriented fibers toward the center in *Pax6*$^{+/+}$ corneas, but these trajectories were sparse and irregular in *Pax6*$^{+/-}$ *mutants. Scale bars* = 500 µm. (**B**) Volumetric quantification of β3-tubulin labelled fibers confirmed that nerve density was reduced by half in mutants. The epithelial fiber volumes in the central area covering 50% of the whole corneal surface are then measured for each stage using Imaris software (n = 5 different animals per group). (**C**) Von Frey testing performed at 3 months revealed a significantly lower basal mechanical sensitivity in *Pax6*$^{+/-}$ mice compared to *Pax6*$^{+/+}$ controls (30% reduction); n = 6 to 8 different animals per group. Each data point represents one animal (biological replicate). Data are represented as mean ± SEM. Statistical analysis was performed using multiple unpaired two-tailed Student's t-tests with false discovery rate control (2-stage Benjamini, Krieger, and Yekutieli procedure). Statistical significance is indicated directly on the figures. (**D**) Overlap of differentially expressed genes

Investigative Ophthalmology & Visual Science

in trigeminal ganglia by sex and genotype. Venn diagram showing the number of genes identified as differentially expressed (irrespective of the direction of change) in four pairwise comparisons ($n = 5$ different animals per group): *Pax6*$^{+/+}$ female mice compared with *Pax6*$^{+/+}$ male mice; *Pax6*$^{+/-}$ female mice compared with *Pax6*$^{+/+}$ female mice; *Pax6*$^{+/-}$ female mice compared with *Pax6*$^{+/-}$ male mice; *Pax6*$^{+/-}$ male mice compared with *Pax6*$^{+/+}$ male mice. Numbers within each region indicate differentially expressed genes meeting the significance threshold for the corresponding comparison; overlapping areas indicate differentially expressed genes shared between comparisons, and the central overlap indicates differentially expressed genes significant in all four comparisons ($n = 5$ different animals per group).

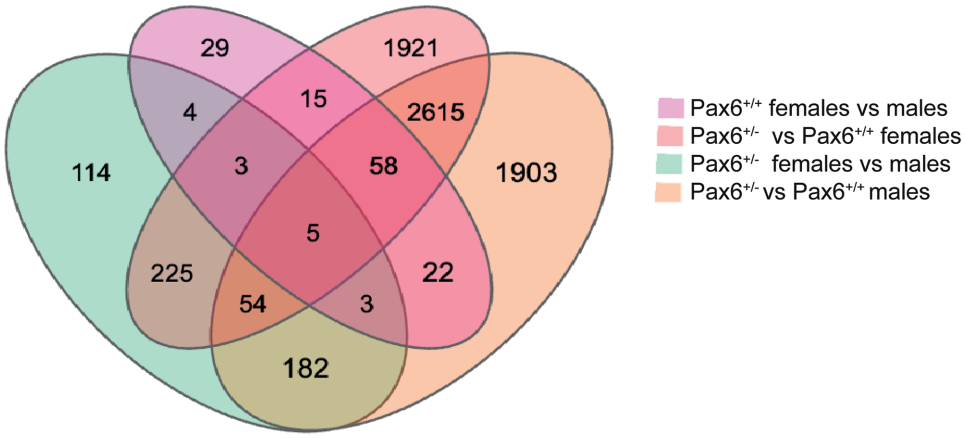

Figure 3. Overlap of differentially expressed genes in mouse corneas by sex and genotype. Venn diagram showing the number of genes identified as differentially expressed (irrespective of direction of change) in four pairwise comparisons. Numbers within each region indicate genes meeting the significance threshold for the corresponding comparison; overlapping areas indicate differentially expressed genes shared between comparisons, and the central overlap indicates differentially expressed genes significant in all four comparisons ($n = 5$ different animals per group).

in females; no intersex difference was evident in *Pax6*$^{+/+}$ (Fig. 6).

At baseline, the *Pax6*$^{+/-}$ tear proteome diverged sharply from *Pax6*$^{+/+}$: female mice showed 125 altered proteins (69 up and 56 down) and male mice showed 62 (28 up and 34 down), with no inversions between sexes (Figs. 7, 8; Supplementary Tables S3A, S3B). Thirteen proteins, including ANP32A, AQP5, and GSTA2, were consistently depleted, suggesting epithelial fragility and reduced water-transport capacity, whereas 16 (e.g., ALDH1A3, FASN, and RAC1) were commonly enriched, indicating shared metabolic activation, oxidative-stress buffering, and cytoskeletal remodeling. Enrichment analyses pointed to loss of adherens-junction together with dysregulated neutrophil-associated pathways (Supplementary Tables S3C–J). Around this core, sex-specific programs diverged: female mices upregulated keratinization modules (e.g., KRT17, KRT19, and KRT15), Rho-GTPase signaling (e.g., RHOA), and neutrophil degranulation, whereas male mice did not show the keratinization signature but instead displayed increased nucleotide-catabolic enzymes (e.g., GDA and UPP1), and Semaphorin-3A signaling (e.g., PLXNA3), a negative regulator of innervation.

After abrasion, *Pax6*$^{+/+}$ tears mounted a coordinated response at 18 hours, with extensive protein modulation (429 in female and 145 in male mice, 121 shared; Supplementary Tables S4A, S4B), characterized by activation of ribosome biogenesis/translation initiation (e.g., RPL18, RPL13A, RPL24, EEF1D, and EEF2) and chaperone-mediated folding (e.g., CCT8), suppression of cornified-envelope/keratinization and epithelial differentiation programs (e.g., KRT12 and ASPRV1), and induction of axon-guidance pathways in both sexes (e.g., CLF1), with a broader repertoire in female mice, accompanied by cytoskeletal remodeling proteins (e.g, RAC1 and RHOA); immune categories were bidirectionally tuned (e.g., upregulation of LCN2 in female mice and downregulation of ANXA2 in both sexes), and sex divergence was modest, with stronger translational activation in female mice and a relatively more prominent glutathione/redox detoxification signature in male mice, e.g., GSTM1 and GPX1 in both sexes, and GLRX3 in male mice; see Supplementary Table S4).

In contrast, *Pax6*$^{+/-}$ tears did not reproduce this robust ribosomal/translation surge, retaining only a partial translational signal in males. Female mutants regulated 250 proteins with downregulation of epithelial development/differentiation and cytoskeletal organization modules (e.g., TJP3, KRT6A, and KRT6B) alongside dysregulated neutrophil/ innate immune secretory programs (e.g. LCN2, LTF, CD14, and C3); male mice modulated 235 proteins with broad Rho-GTPase/cytoskeletal remodeling and vesicle-traffiking activation (e.g., RHOA, RAC1, and SAR1B), glycolytic and nucleotide-catabolic acceleration (e.g., GPI, ALDOA, PGAM1, and PNP), and upregulation of cornified-envelope components (e.g., SPRR1A, KRT1, and KRT10; see Supplementary Table S5). Axonogenesis signals in mutants were sex-divergent and discordant: male mice upregulated Eph/Ephrin and axon-guidance pathways, but these were accompanied by axonal growth inhibition programs, associated with cytoskeletal remodeling (e.g., CFL1 and PFN1), and female mice showed no significant enrichment of axon-guidance categories.

Direct genotype comparisons at 18 hours showed that, relative to *Pax6*$^{+/+}$, *Pax6*$^{+/-}$ tears exhibited reduced translation-related signatures, predominantly in male mice (e.g., RPS 10 in female mice, and RPS28, RPS4X, RPS23, EEF1A1, and EIF6 in male mice), inhibition of axon-guidance/axon-related transport programs (e.g., KIF5B in

Investigative Ophthalmology & Visual Science

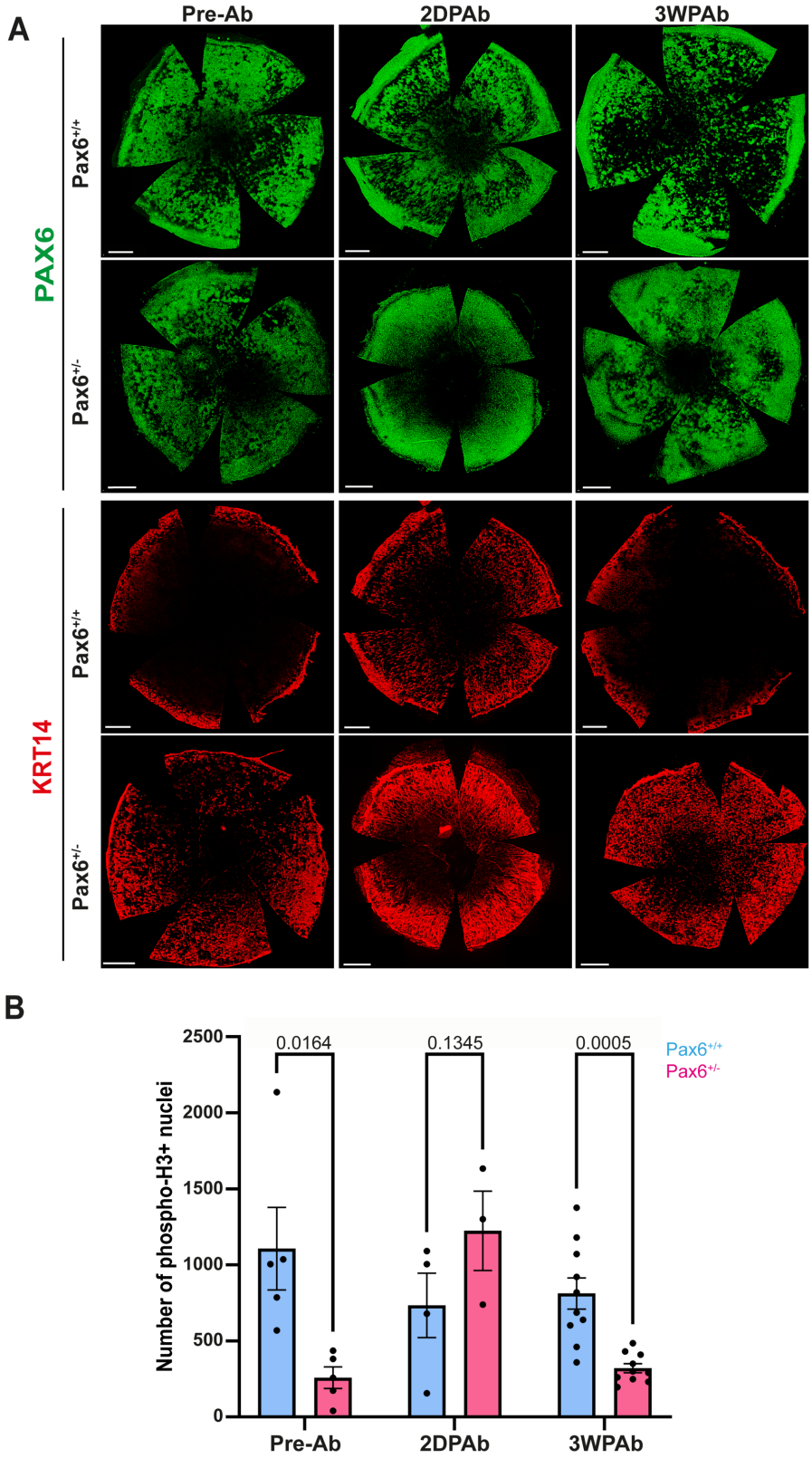

Figure 4. Defective corneal epithelial repair, patterning, and proliferative response following abrasion in *Pax6*$^{+/-}$ mutants. (**A**) PAX6 expression before and after corneal abrasion. At 3 months, pre-abrasion, PAX6 immunostaining displays a comparable pattern and intensity in *Pax6*$^{+/-}$ and *Pax6*$^{+/+}$ *corneas*. At 2 days post-abrasion, *Pax6*$^{+/+}$ regains the characteristic patchy, high-intensity signal; *Pax6*$^{+/-}$ shows a uniform, reduced signal. At 3 weeks post-abrasion, *Pax6*$^{+/+}$ returns to the patchy pattern; *Pax6*$^{+/-}$ remains uniformly diminished. *Scale bars* = 500 µm. Time notation: Ab = abrasion; P = post; D = days; W = weeks. (**B**) Post-abrasion corneal epithelial reorganization is impaired in *Pax6*$^{+/-}$ mutants. Whole-mount KRT14 staining at the indicated post-abrasion time points shows recovery

Investigative Ophthalmology & Visual Science

of peripheral-basal patterning in *Pax6*$^{+/+}$ corneas, whereas *Pax6*$^{+/-}$ corneas remain mispatterned with an expanded, disorganized KRT14 signal and incomplete centripetal reorganization. *Scale bars* = 500 µm. Time notation: Ab = abrasion; P = post ; D = days; W = weeks. (**C**) Impaired proliferative response after corneal abrasion in *Pax6*$^{+/-}$ mutants. Quantification of pH3^{+} nuclei shows reduced basal proliferation in *Pax6*$^{+/-}$ corneas compared to *Pax6*$^{+/+}$ before abrasion. By 3 weeks post-abrasion, proliferation remains significantly reduced in *Pax6*$^{+/-}$ compared to *Pax6*$^{+/+}$, reflecting a sustained proliferative deficit. Each data point represents one animal (biological replicate, n = 3–8 different animals per group). Data are represented as mean ± SEM. Statistical analysis was performed using multiple unpaired two-tailed Student's *t*-tests with false discovery rate control (2-stage Benjamini, Krieger, and Yekutieli procedure). Statistical significance is indicated directly on the figures. Time notation: Ab = abrasion; P = post; D = days; W = weeks.

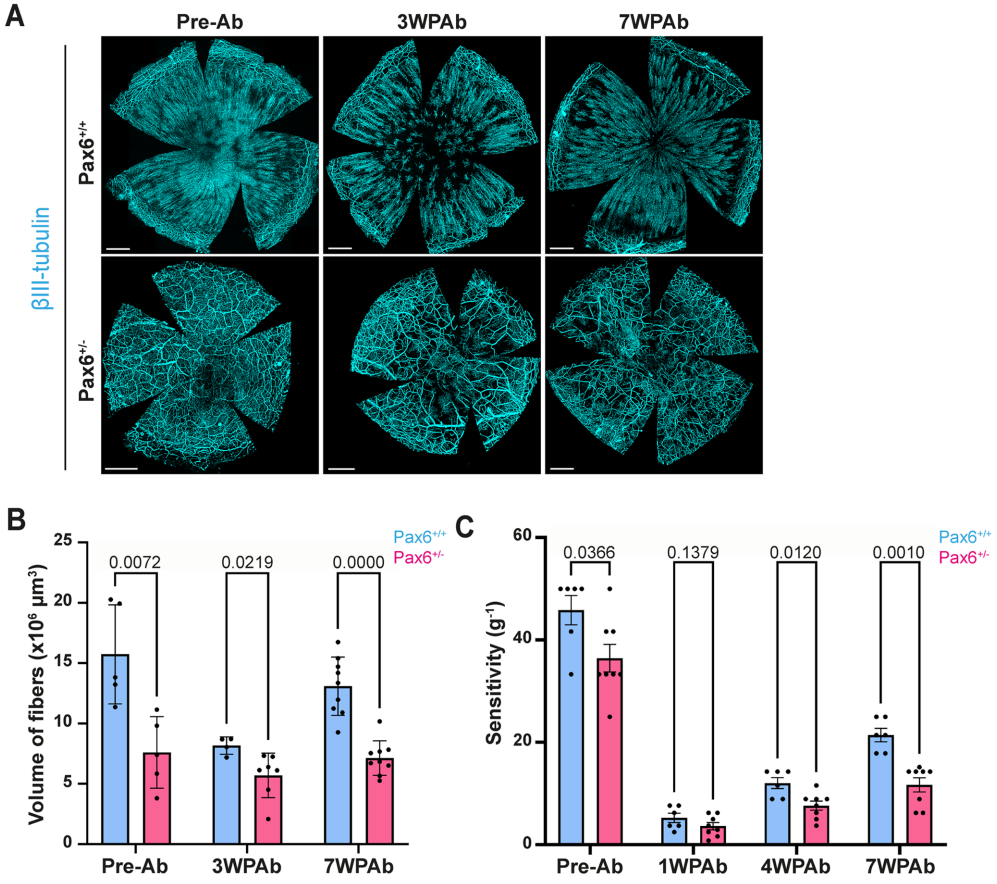

Figure 5. Delayed and incomplete corneal reinnervation and sensory recovery after abrasion in *Pax6*$^{+/-}$ mutants. (**A**) β3-tubulin immunostaining shows that after abrasion, *Pax6*$^{+/+}$ corneas progressively regenerate thin radially oriented fibers that converge into a central vortex by 7 weeks post-abrasion. In contrast, *Pax6*$^{+/-}$ corneas fail to re-establish the subbasal small-fiber network, displaying the same disorganized and reduced innervation pattern already present at baseline. (**B**) Volume quantification of β3-tubulin positive epithelial fibers shows a 50% deficit in mutants at baseline (pre-abrasion), and 40% at 7 weeks post-abrasion (n = 4–9 different animals per group). (**C**) Epicritic mechanical sensitivity (von Frey) recovers only partially in *Pax6*$^{+/+}$ (50% of baseline at 7WPA). The mutant deficit appears by 4 weeks post-abrasion and persists at 7 weeks at 30% below *Pax6*$^{+/+}$ (n = 6–8 different animals per group). Each data point represents one animal (biological replicate). Data are represented as mean ± SEM. Statistical analysis was performed using multiple unpaired two-tailed Student's *t*-tests with false discovery rate control (2-stage Benjamini, Krieger, and Yekutieli procedure). Statistical significance is indicated directly on the figures as dots. *Scale bars* = 300 µm. Time notation: Ab = abrasion; P = post ; D = days; W = weeks.

male mice and MYO6 in female mice) and oxidative stress-response pathways (e.g., PRDX6 and TXNDC17), more consistently enriched in female mice (see Supplementary Table S6). Conversely, they over-activated innate (e.g., LCN2 and S100A9 in male mice, and IL1RAP, MIF, and C3 in female mice) and keratinization (e.g., KRT1, KRT10, and SPRR1A in female mice, and KRT17 in male mice) pathways in both sexes; additionally, female mutants showed increased epidermal differentiation (e.g., KRT13 and SCEL), with a parallel rise in endothelial cell migration–related terms (e.g EGF and LGALS3), whereas male mutants altered JAK–STAT signaling while enhancing Rho-GTPase/actin remodeling (e.g., RAC1, CFL1, ARPC2, and TLN1) and glycolytic/nucleotide-catabolic flux (e.g., GPI, PGK1, PGAM1, and PNP; see Supplementary Table S6).

Among differentially expressed proteins, ALDH3A1 emerged as a common, significantly downregulated hit across three *Pax6*$^{+/-}$ versus *Pax6*$^{+/+}$ contrasts (male post-abrasion, female pre-abrasion, and female post-abrasion).

Discussion

As observed in patients with aniridia, phenotypic expressivity in *Pax6*$^{+/-}$ mice was heterogeneous across the cohort, indicating variable penetrance of individual features but a consistent overall disruption of ocular development. AAK

Investigative Ophthalmology & Visual Science

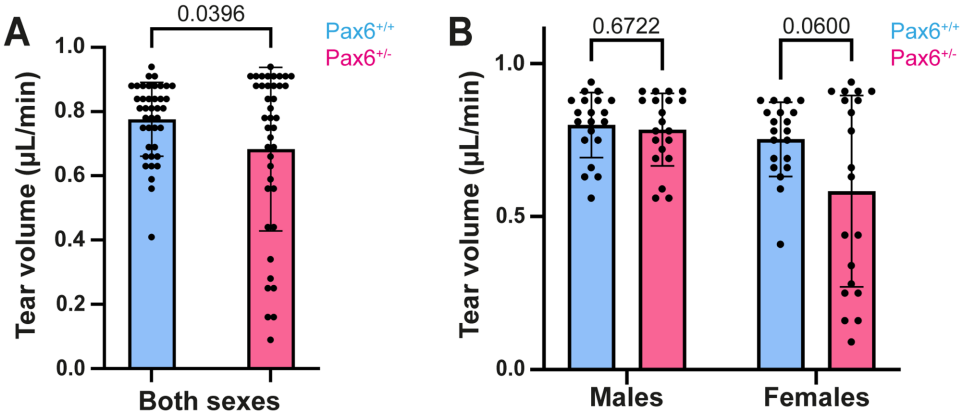

Figure 6. Impact of Pax6 genotype and sex on tear volume. Tear volume is significantly reduced in *Pax6*$^{-/-}$ mice compared to *Pax6*$^{+/+}$ controls, and shows a trend toward reduction in female *Pax6*$^{+/-}$ mice compared to female *Pax6*$^{+/+}$ controls ($P = 0.06$). (**A**) Global effect of Pax6 genotype on tear secretion rate (µL/min). (**B**) Effect of Pax6 genotype analyzed separately in male and female mice. For each animal, tears from both eyes were separately collected. Sample sizes are indicated on the graphs by *dots* ($n = 18$ eyes per group). Data are represented as mean ± SEM. Statistical analysis was performed using multiple unpaired two-tailed Student's *t*-tests with false discovery rate control (2-stage Benjamini, Krieger, and Yekutieli procedure). Statistical significance is indicated directly on the figures.

is a multifactorial disorder in which epithelial dysmaturation, sensory denervation, and chronic inflammation interact to drive progressive corneal failure.[3,36] Using a Pax6-haploinsufficient mouse model, we examined baseline ocular surface pathology and repair dynamics following abrasion in order to clarify the mechanisms underlying AAK. The central findings of this study are the coexistence of epithelial dysmaturation, sensory denervation, and impaired tissue restoration after injury in Pax6-haploinsufficient corneas, whereas transcriptomic and tear proteomic datasets provide complementary molecular context.

Our epithelial readouts (KRT12/KRT14) indicate incomplete differentiation with persistence of a progenitor-like state, establishing PAX6 as essential for corneal epithelial maturation and territorial organization, consistent with reduced KRT12 and altered ΔNp63/GPHA2 expression in *Pax6*$^{+/Sey}$ corneas.[37] Homeostasis was already perturbed centrally by 2 weeks, with a sustained mitotic deficit persisting to 3 months. Apparent discrepancies with reports of increased turnover in *Pax6*$^{+/Sey}$ lines may be reconciled by methodological and biological differences. Methodologically, we quantified proliferation strictly within the central 50% of the cornea (CROP50), whereas previous studies examined the entire epithelium or mid-corneal sections without central restriction. Denominator selection may vary with regional epithelial thickness, which is greater centrally, and with genotype-specific epithelial thinning, potentially inflating labeling fractions outside the center. In addition, pH3 marks the brief M phase, whereas Ki-67 spans G1-S-G2-M and BrdU captures S phase or cumulative cycling; thus, prolongation of S/G2 or activation of a G2/M checkpoint may increase Ki-67 or BrdU labeling while reducing pH3 positivity.[38–41] Biologically, our earliest assessments were performed at 2 weeks, whereas increased indices in previous reports peaked at 6 to 12 weeks. Allelic and genetic background effects, including Sey on CBA/Ca or C3H backgrounds, may also influence the timing and magnitude of these changes. Taken together, these considerations suggest that an early central mitotic deficit may precede, and later coexist with, compensatory and more peripheral hyperproliferation, potentially contributing to limbal stem cell dysfunction.[3,36]

Inflammation was both strikingly early and persistent: CD45+ cells were increased from eyelid opening, at 2 weeks, and remained elevated thereafter. Although a basal population of CD45+ resident leukocytes is normally present in healthy corneas, the marked and sustained increase observed in *Pax6*$^{+/-}$ mice indicates an early amplification of this physiological immune compartment rather than mere baseline immune surveillance.[42–44] This precedes the earliest time points reported in *Pax6*$^{+/Sey}$ (129S1/SvImJ) corneas, where stromal infiltrates were detected from 1 month onward in a subset of animals,[37] and mirrors human AAK in which central MHC-II+ dendritic cells accumulate before stromal remodeling.[3] These findings support ultra-early immune activation as a plausible contributor to epithelial dysfunction. The timing and persistence of this response suggests that reduced PAX6 dosage disrupts ocular surface homeostasis at, or immediately after, eyelid opening, coinciding with environmental exposure, and reflects a sustained inability to resolve inflammation over time.

Sensory innervation was profoundly altered, with loss and disorganization of fine epithelial fibers, attenuation of TRPM8+ terminals, and reduced epicritic sensitivity. Because corneal Aδ- and C-fiber somata reside in the TG, we profiled the TG transcriptome and found minimal differential expression, suggesting that the defect is encoded locally at the cornea rather than at the neuronal soma. Overall, these findings support a locally coordinated pathology rather than a primary neuronal defect. Given the established roles of PAX6 in morphogenesis, matrix patterning, and trophic cue expression,[45–48] local deficits in guidance and maintenance likely underlie denervation. This denervation may in turn reduce blinking, tearing, and trophic support, thereby further destabilizing the ocular surface.[49–51]

Corneal transcriptomics revealed modest sex differences in *Pax6*$^{+/+}$ tissue but a pronounced sex-dependent divergence under haploinsufficiency. Male and female mice dysregulated largely distinct gene sets that nevertheless converged on shared programs involving inflammation and ECM remodeling. Sex-specific modules, including metabolic suppression in female mice (xenobiotic/cytochrome P450, glutathione, and retinol) and enhanced innate immunity coupled to repression of sensory pathways in male mice,

Investigative Ophthalmology & Visual Science

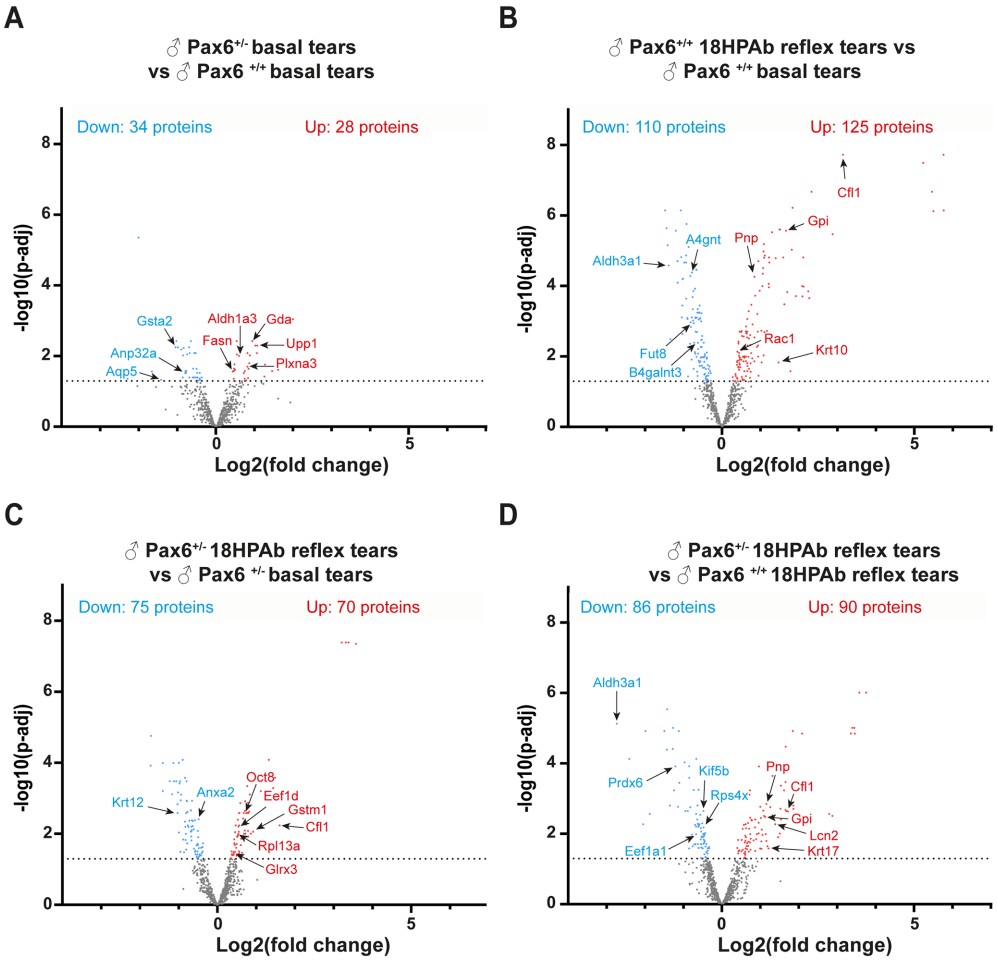

Figure 7. Impact of *Pax6* genotype, and corneal abrasion on tear secretion and proteome in male mice. (**A–D**) Volcano plots representing differential tear protein expression identified by mass spectrometry (n = 10 different animals, 5 pooled samples per group) under the indicated conditions. **A** Male mice *Pax6*$^{+/-}$ versus *Pax6*$^{+/+}$ at baseline (basal tears). **B** Male mice *Pax6*$^{+/-}$ 18 hours post-abrasion versus basal. **C** Male mice *Pax6*$^{+/-}$ 18 hours post-abrasion versus basal. **D** Male mice *Pax6*$^{+/-}$ vs. *Pax6*$^{+/+}$ 18 hours post-abrasion. The *horizontal dotted line* marks the significance threshold; *vertical dotted lines* delimit fold-change cutoffs; proteins above/below the cutoffs are *highlighted*, whereas others appear in *grey*. Statistical analysis using a *t*-test with permutated-based FDR of 0.05. Bottom volcano plots are represented with *q* values. Statistical analysis using a Benjamini–Hochberg *P* value correction.

suggest that endocrine and/or chromosomal factors modulate how PAX6 dosage is translated into ocular surface pathology.[52–54]

Wound-healing analyses further refine these mechanisms. Despite comparable macroscopic closure times, *Pax6*$^{+/-}$ corneas failed to re-establish normal epithelial identity: PAX6 staining remained faint and uniform, KRT14 persisted centrally, and the baseline proliferation deficit re-emerged. Nerve regeneration was slow even in wild-type corneas and remained durably inferior in mutants, paralleling persistent sensory loss reminiscent of clinical observations.[3,55] These findings underscore that epithelial resurfacing and restoration of tissue identity are distinct processes. They suggest that PAX6 may be dispensable for resurfacing per se but essential for appropriate maturation, proliferation control, and coordinated epithelial-stromal-neural repair, consistent with prior evidence that PAX6 supports junctional stability, regulates stromal apoptosis and MMP9, and that its nuclear dysfunction imprints a chronic wound-like state.[25,26,56,57]

The lacrimal axis emerged as both sensitive to PAX6 dosage and sexually modulated. Tear volume deficits tended to be female-driven, and proteomic analyses revealed a baseline loss of structural and antioxidant components together with enrichment of stress- and metabolism-related factors, consistent with a fragile, oxidation-prone barrier. Male mutants showed increased Semaphorin-3-related proteins, a pathway previously implicated in axonal guidance and repulsion.[58] Following abrasion, *Pax6*$^{+/+}$ ears activated translation and axon-guidance programs, whereas mutants failed to fully reproduce this response and instead showed exaggerated neutrophil and platelet degranulation. This immune skew is consistent with observations in human AAK, in which mature dendritic cells accumulate centrally early in disease,[3] and aligns with keratinization and cornification signatures consistent with epithelial fragility and metaplasia.[59] Dysregulation of axon-guidance and cytoskeletal pathways may also contribute to impaired neural repair.[60] These findings argue that tear composition may actively contribute to ocular surface homeostasis rather than merely reflect it, although functional effects cannot be inferred directly from protein abundance alone. This interpretation is consistent with PAX6 control of corneal

Investigative Ophthalmology & Visual Science

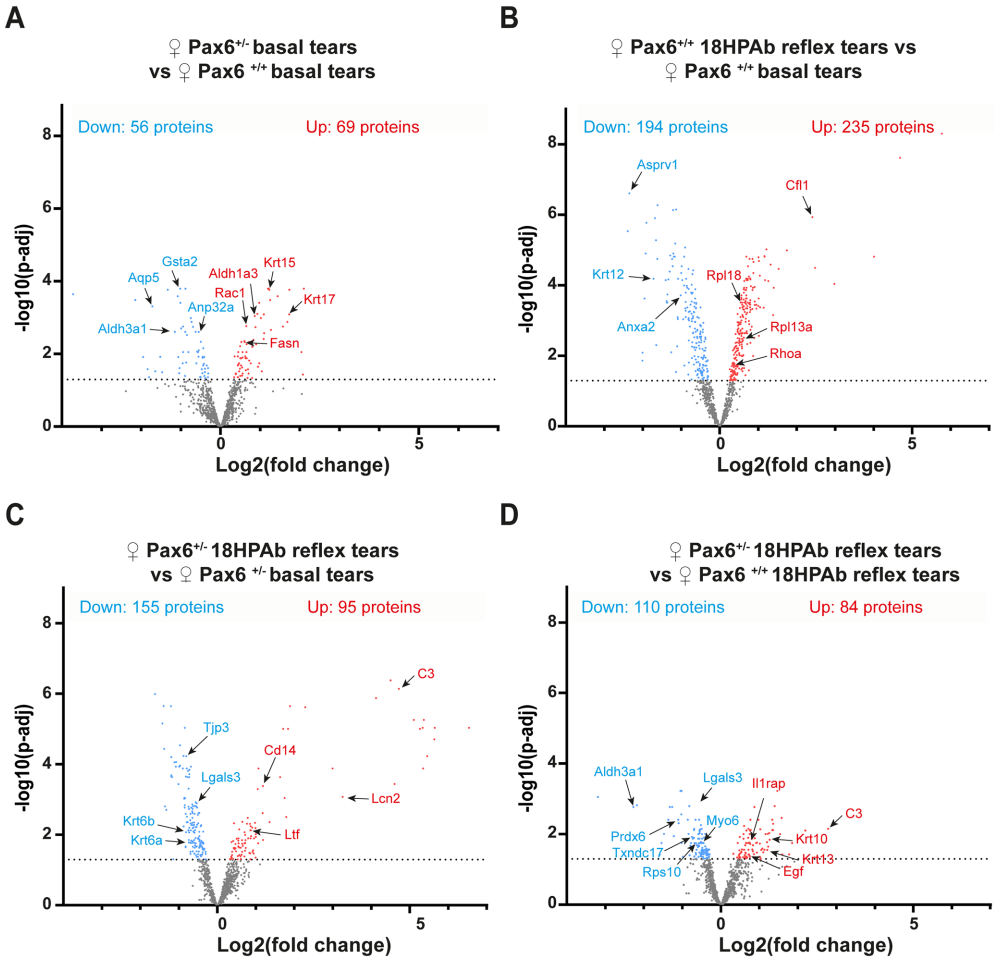

Figure 8. Impact of *Pax6* genotype, and corneal abrasion on tear secretion and proteome in female mice. (**A–D**) Volcano plots representing differential tear protein expression identified by mass spectrometry (n = 10 different animals, 5 pooled samples per group) under the indicated conditions. **A** Female mice Pax6$^{+/-}$ vs Pax6$^{+/+}$ at baseline (basal tears). **B** Female mice *Pax6*$^{+/+}$ 18 hours post-abrasion versus basal. **C** Female mice *Pax6*$^{+/-}$ 18 hours post-abrasion versus basal. **D** Female mice Pax6$^{+/-}$ versus Pax6$^{+/+}$ 18 hours post-abrasion. The *horizontal dotted line* marks the significance threshold; *vertical dotted lines* delimit fold-change cutoffs; proteins above/below the cutoffs are *highlighted*, while others appear in *grey*. Statistical analysis using a *t*-test with permutated-based FDR of 0.05. Bottom volcano plots are represented with q values. Statistical analysis using a Benjamini–Hochberg P value correction.

morphogenesis and innervation, as well as lacrimal development, and with human lacrimal organoid data showing preserved progenitor populations but defective ductal differentiation and reduced AQP5 and exocytosis machinery following PAX6 loss.[23,61,62] Sex-stratified proteomic responses further support endocrine modulation of secretion and composition.[63–66] In *Pax6*$^{+/+}$ mice, female mice mounted a higher-amplitude response dominated by translation and axon-guidance pathways; under haploinsufficiency, the balance shifted toward inflammation and keratinization in female mice, whereas male mice showed metabolic and vesicle-trafficking reprogramming together with altered JAK-STAT signaling, consistent with epithelial barrier impairment.

Because pathway enrichment analyses are based on protein abundance, they identify associated biological processes but do not establish functional activity or causality. Functional validation will therefore be required to determine the mechanistic contribution of these pathways.

The decrease in ALDH3A1 is consistent with evidence that PAX6 directly regulates its corneal transcription.[67–69] Given the role of ALDH3A1 in detoxifying lipid peroxidation-derived aldehydes, protecting against oxidative and UV injury, and acting as a major corneal crystallin with structural contributions, its loss may plausibly compromise epithelial homeostasis and optical clarity.[70–72] Concordant observations in humans support a shared mechanism linking epithelial identity, antioxidant defense, and transparency, thereby nominating ALDH3A1 as a priority pathophysiological target in PAX6-related aniridia keratopathy.[73]

Several limitations related to the genetic model should be acknowledged. We used a conditional Pax6^{tm1Ued} allele in which recombination was driven by a CMV-Cre transgene, inducing strong and widespread Cre activity across tissues early in development.[74,75] Consequently, the resulting phenotype reflects systemic Pax6 haploinsufficiency rather than tissue-restricted deletion. Although this approach provides a robust model of dosage deficiency comparable to human PAX6 heterozygosity, it does not allow discrimination between cell-autonomous corneal effects and indirect contributions from other ocular or systemic compartments,

Investigative Ophthalmology & Visual Science

including neural crest derivatives, trigeminal pathways, or lacrimal tissues.

Most pathogenic human *PAX6* variants associated with classical aniridia are truncating mutations that result in nonsense-mediated decay and functional haploinsufficiency.[76] Our conditional deletion, which generates a null allele in heterozygosity, therefore models the predominant molecular mechanism observed in patients.[76] Nevertheless, it does not encompass the full allelic spectrum of PAX6-related disease, including hypomorphic or regulatory variants that may produce distinct phenotypic trajectories.

Although corneal denervation and epithelial abnormalities coexist in our model, the present study does not directly test whether neural defects drive epithelial dysmaturation. Establishing causality will require targeted manipulation of corneal innervation or neurotrophic signaling pathways.

Compared with the Javidjam *Pax6*$^{+/Sey}$ (129S1/SvImJ) model, both systems capture the cardinal axes of AAK, including epithelial dysmaturation with altered KRT12/KRT14 territories, subbasal plexus disruption, early immune infiltration, and barrier compromise. Their trajectories nevertheless differ. Javidjam et al. describe a mild neonatal onset followed by progressive worsening over several months, with basement membrane collagen IV loss and increasing basal Ki-67 with disease grade. Our model instead highlights initiation events beginning at eyelid opening, including an early central deficit in mitotic entry, robust early immune infiltration, marked neurotrophic defects, and explicit impairments in repair organization.

By integrating corneal transcriptomics with tear proteomics, we link epithelial and neural alterations to lacrimal remodeling and uncover sex-specific molecular patterns. This Pax6-haploinsufficient model therefore complements existing systems by capturing early pathogenic processes and providing a mechanistic framework for the exploration of candidate biomarkers.

Collectively, our findings show that Pax6 haploinsufficiency recapitulates key pathological axes of human aniridia-associated keratopathy, positioning epithelial dysmaturation, neurotrophic impairment, and inflammation as core components of the phenotype, with tear film abnormalities acting as an additional modulatory layer beyond stem cell deficiency alone.[77] This model provides an integrated experimental platform to dissect the temporal interactions among these mechanisms and to evaluate strategies aimed at improving or refining existing therapeutic approaches for AAK, highlighting inflammation, neurotrophic support, and tear film quality as candidate therapeutic targets.

Acknowledgments

The authors thank the MRI-DBS imaging facility, member of the France-BioImaging national infrastructure. We also thank the personnel of the INM animal core facility, members of the Animal Facility Network in Montpellier (RAM).

Supported by the Fondation Groupama, ATIP-Avenir program, Inserm, the Région Occitanie, ANR (ANR-21-CE17-0061, TeFi-CoPa), and FRM (REP202110014140).

Mass spectrometry proteomic and epitranscriptomic experiments were carried out using the facilities of the Montpellier Proteomics Platform (PPM, BioCampus Montpellier), a member of the national Proteomics French Infrastructure (ProFI UAR 2048), supported by the French National Research Agency (ANR-24-INBS-0015, Investments for the future F2030). supported by the French National Research Agency (ANR-10-INBS-04, Investments for the future»).

Ethics Declarations: All the experiments conducted on mice were approved by the local ethical committee and the Ministère de la Recherche et de l'Enseignement Supérieur (authorization 2016080510211993 version 2). All of the procedures were carried out in accordance with the French regulation for the animal procedure (French decree 2013-118) and with specific European Union guidelines for the protection of animal welfare (Directive 2010/63/EU). The study adheres to the ARRIVE guidelines and the ARVO Statement for the Use of Animals in Ophthalmic and Vision Research.

Author Contributions: Conceptualization: M.W. and F.M.; Methodology: M.W., M.G., N.F., D.T., J.V., J.K., L.F., C.H., D.B.G., V.D., C.D., M.P., and F.M.; Validation: M.W., M.G., and F.M.; Formal analysis: M.W., M.G., N.F., J.K., and L.F.; Data analysis: M.W., M.G., and F.M.; Writing: M.W., M.G., N.F., D.T., J.V., J.K., L.F., C.H., D.B.G., V.D., C.D., M.P., and F.M.; Supervision: M.P. and F.M.; Project administration: F.M.; Funding acquisition: F.M.

Disclosure: **M. Willems**, None; **M. Girard**, None; **N. Feret**, None; **D. Touchet**, None; **J. Vialaret**, None; **J. Kindermans**, None; **L. Fichter**, None; **C. Hirtz**, None; **D. Bremond-Gignac**, None; **V. Daien**, None; **C. Delettre**, None; **M. Pequignot**, None; **F. Michon**, None

References

1. Tibrewal S, Ratna R, Gour A, et al. Clinical and molecular aspects of congenital aniridia - a review of current concepts. *Indian J Ophthalmol*. 2022;70(7):2280–2292.
2. Daruich A, Duncan M, Robert MP, et al. Congenital aniridia beyond black eyes: from phenotype and novel genetic mechanisms to innovative therapeutic approaches. *Prog Retin Eye Res*. 2023;95:101133.
3. Lagali N, Wowra B, Fries FN, et al. Early phenotypic features of aniridia-associated keratopathy and association with PAX6 coding mutations. *Ocul Surf*. 2020;18(1):130–140.
4. Fries FN, Moslemani K, Utheim TP, Seitz B, Käsmann-Kellner B, Lagali NS. Early ocular surface and tear film status in congenital aniridia indicates a supportive treatment window. *Br J Ophthalmol*. 2023;108(1):30–36.
5. Voskresenskaya A, Pozdeyeva N, Vasilyeva T, et al. Clinical and morphological manifestations of aniridia-associated keratopathy on anterior segment optical coherence tomography and in vivo confocal microscopy. *Ocul Surf*. 2017;15(4):759–769.
6. Eghrari AO, Riazuddin SA, Gottsch JD. Chapter Two - Overview of the cornea: structure, function, and development. *Prog Mol Biol Transl Sci*. 2015;134:7–23.
7. Henriksson JT, McDermott AM, Bergmanson JPG. Dimensions and morphology of the cornea in three strains of mice. *Invest Ophthalmol Vis Sci*. 2009;50(8):3648–3654.
8. Nasser W, Amitai-Lange A, Soteriou D, et al. Corneal-committed cells restore the stem cell pool and tissue boundary following injury. *Cell Rep*. 2018;22(2):323–331.
9. Sridhar M. Anatomy of cornea and ocular surface. *Indian J Ophthalmol*. 2018;66(2):190.
10. Jamali A, Kenyon B, Ortiz G, et al. Plasmacytoid dendritic cells in the eye. *Prog Retin Eye Res*. 2021;80:100877.
11. Foulsham W, Coco G, Amouzegar A, Chauhan SK, Dana R. When clarity is crucial: regulating ocular surface immunity. *Trends Immunol*. 2018;39(4):288–301.
12. Liu J, Li Z. Resident innate immune cells in the cornea. *Front Immunol*. 2021;12:620284.

13. Marfurt C, Anokwute MC, Fetcko K, et al. Comparative anatomy of the mammalian corneal subbasal nerve plexus. *Invest Ophthalmol Vis Sci*. 2019;60(15):4972.
14. Müller LJ, Marfurt CF, Kruse F, Tervo TMT. Corneal nerves: structure, contents and function. *Exp Eye Res*. 2003;76(5):521–542.
15. von Thun U, Hohenstein-Blaul N, Funke S, Grus FH. Tears as a source of biomarkers for ocular and systemic diseases. *Exp Eye Res*. 2013;117:126–137.
16. Iwata S. Chemical composition of the aqueous phase. *Int Ophthalmol Clin*. 1973;13(1):29–46.
17. Klenkler B, Sheardown H, Jones L. Growth factors in the tear film: role in tissue maintenance, wound healing, and ocular pathology. *Ocul Surf*. 2007;5(3):228–239.
18. Whitson JT, Liang C, Godfrey DG, et al. Central corneal thickness in patients with congenital aniridia. *Eye Contact Lens*. 2005;31(5):221–224.
19. Latta L, Figueiredo FC, Ashery-Padan R, et al. Pathophysiology of aniridia-associated keratopathy: developmental aspects and unanswered questions. *Ocul Surf*. 2021;22:245–266.
20. Volland S, Esteve-Rudd J, Hoo J, Yee C, Williams DS. A comparison of some organizational characteristics of the mouse central retina and the human macula. *PLoS One*. 2015;10(4):e0125631.
21. Loiseau A, Raîche-Marcoux G, Maranda C, Bertrand N, Boisselier E. Animal models in eye research: focus on corneal pathologies. *Int J Mol Sci*. 2023;24(23):16661.
22. Abdolkarimi D, Cunha DL, Lahne M, Moosajee M. PAX6 disease models for aniridia. *Indian J Ophthalmol*. 2022;70(12):4119–4129.
23. Makarenkova HP, Ito M, Govindarajan V, et al. FGF10 is an inducer and Pax6 a competence factor for lacrimal gland development. *Development*. 2000;127(12):2563–2572.
24. Ou J, Lowes C, Collinson JM. Cytoskeletal and cell adhesion defects in wounded and Pax6$^{+/-}$ corneal epithelia. *Invest Ophthalmol Vis Sci*. 2010;51(3):1415–1423.
25. Ou J, Walczysko P, Kucerova R, et al. Chronic wound state exacerbated by oxidative stress in Pax6$^{+/-}$ aniridia-related keratopathy. *J Pathol*. 2008;215(4):421–430.
26. Ramaesh T, Ramaesh K, Leask R, et al. Increased apoptosis and abnormal wound-healing responses in the heterozygous Pax6$^{+/-}$ mouse cornea. *Invest Ophthalmol Vis Sci*. 2006;47(5):1911.
27. Leiper LJ, Ou J, Walczysko P, et al. Control of patterns of corneal innervation by Pax6. *Invest Ophthalmol Vis Sci*. 2009;50(3):1122.
28. Simpson TI, Pratt T, Mason JO, Price DJ. Normal ventral telencephalic expression of Pax6 is required for normal development of thalamocortical axons in embryonic mice. *Neural Dev*. 2009;4(1):19.
29. Kalha S, Shrestha B, Sanz Navarro M, Jones KB, Klein OD, Michon F. Bmi1+ progenitor cell dynamics in murine cornea during homeostasis and wound healing. *Stem Cells*. 2018;36(4):562–573.
30. Meneux L, Caballero A, Boukhaddaoui H, Michon F. Three strategies to induce neurotrophic keratitis and nerve regeneration in murine cornea. *J Vis Exp*. 2023;(202):66182.
31. Gautier B, Meneux L, Feret N, et al. AAV2/9-mediated gene transfer into murine lacrimal gland leads to a long-term targeted tear film modification. *Mol Ther Methods Clin Dev*. 2022;27:1–16.
32. Li R, Li Y, Kristiansen K, Wang J. SOAP: short oligonucleotide alignment program. *Bioinformatics*. 2008;24(5):713–714.
33. Langmead B, Salzberg SL. Fast gapped-read alignment with Bowtie 2. *Nat Methods*. 2012;9(4):357–359.
34. Love MI, Huber W, Anders S. Moderated estimation of fold change and dispersion for RNA-seq data with DESeq2. *Genome Biol*. 2014;15(12):550.
35. Zieske J. Corneal development associated with eyelid opening. *Int J Dev Biol*. 2004;48:903–911.
36. Lagali N, Wowra B, Dobrowolski D, Utheim TP, Fagerholm P, Wylegala E. Stage-related central corneal epithelial transformation in congenital aniridia-associated keratopathy. *Ocul Surf*. 2018;16(1):163–172.
37. Javidjam D, Moustardas P, Abbasi M, Dashti A, Rautavaara Y, Lagali N. A human-like model of aniridia-associated keratopathy for mechanistic and therapeutic studies. *JCI Insight*. 2024;10(2):e183965.
38. Scholzen T, Gerdes J. The Ki-67 protein: from the known and the unknown. *J Cell Physiol*. 2000;182(3):311–322.
39. Davis J, Duncan MK, Robison WG, Piatigorsky J. Requirement for Pax6 in corneal morphogenesis: a role in adhesion. *J Cell Sci*. 2003;116(11):2157–2167.
40. Kim JY, Jeong HS, Chung T, et al. The value of phosphohistone H3 as a proliferation marker for evaluating invasive breast cancers: A comparative study with Ki67. *Oncotarget*. 2017;8(39):65064–65076.
41. Taupin P. BrdU immunohistochemistry for studying adult neurogenesis: paradigms, pitfalls, limitations, and validation. *Brain Res Rev*. 2007;53(1):198–214.
42. Liu J, Li Z. Resident innate immune cells in the cornea. *Front Immunol*. 2021;12:620284.
43. Jamali A, Kenyon B, Ortiz G, et al. Plasmacytoid dendritic cells in the eye. *Prog Retin Eye Res*. 2021;80:100877.
44. Foulsham W, Coco G, Amouzegar A, Chauhan SK, Dana R. When clarity is crucial: regulating ocular surface immunity. *Trends Immunol*. 2018;39(4):288–301.
45. McKenna CC, Munjaal RP, Lwigale PY. Distinct roles for neuropilin1 and neuropilin2 during mouse corneal innervation. *PLoS One*. 2012;7(5):e37175.
46. Collinson JM, Chanas SA, Hill RE, West JD. Corneal development, limbal stem cell function, and corneal epithelial cell migration in the Pax6$^{+/-}$ mouse. *Invest Ophthalmol Vis Sci*. 2004;45(4):1101.
47. Collinson JM, Quinn JC, Hill RE, West JD. The roles of Pax6 in the cornea, retina, and olfactory epithelium of the developing mouse embryo. *Dev Biol*. 2003;255(2):303–312.
48. McKenna CC, Lwigale PY. Innervation of the mouse cornea during development. *Invest Ophthalmol Vis Sci*. 2011;52(1):30.
49. He J, Bazan NG, Bazan HEP. Mapping the entire human corneal nerve architecture. *Exp Eye Res*. 2010;91(4):513–523.
50. Belmonte C, Nichols JJ, Cox SM, et al. TFOS DEWS II pain and sensation report. *Ocul Surf*. 2017;15(3):404–437.
51. Kowtharapu BS, Stachs O. Corneal cells: fine-tuning nerve regeneration. *Curr Eye Res*. 2020;45(3):291–302.
52. Pikuleva IA. Challenges and opportunities in P450 research on the eye. *Drug Metab Dispos*. 2023;51(10):1295–1307.
53. McKay TB, Priyadarsini S, Karamichos D. Sex hormones, growth hormone, and the cornea. *Cells*. 2022;11(2):224.
54. Song YS, Annalora AJ, Marcus CB, Jefcoate CR, Sorenson CM, Sheibani N. Cytochrome P450 1B1: a key regulator of ocular iron homeostasis and oxidative stress. *Cells*. 2022;11(19):2930.
55. van Velthoven AJH, Utheim TP, Notara M, et al. Future directions in managing aniridia-associated keratopathy. *Surv Ophthalmol*. 2023;68(5):940–956.
56. Yu F, Zhang W, Yan C, et al. PAX6, modified by SUMOylation, plays a protective role in corneal endothelial injury. *Cell Death Dis*. 2020;11(8):683.

Investigative Ophthalmology & Visual Science

57. Sivak JM, West-Mays JA, Yee A, Williams T, Fini ME. Transcription factors Pax6 and AP-2alpha interact to coordinate corneal epithelial repair by controlling expression of matrix metalloproteinase gelatinase B. *Mol Cell Biol*. 2004;24(1):245–257.
58. Kubilus JK, Linsenmayer TF. Developmental guidance of embryonic corneal innervation: roles of Semaphorin3A and Slit2. *Dev Biol*. 2010;344(1):172–184.
59. Ljubimov AV, Saghizadeh M. Progress in corneal wound healing. *Prog Retin Eye Res*. 2015;49:17–45.
60. Csorba A, Kormányos K, Csidey M, et al. Examination of subbasal nerve plexus and central corneal stromal microstructure in subjects with congenital aniridia, using in vivo confocal laser scanning microscopy. *Curr Eye Res*. 2024;49(6):582–590.
61. Bannier-Hélaouët M, Post Y, Korving J, et al. Exploring the human lacrimal gland using organoids and single-cell sequencing. *Cell Stem Cell*. 2021;28(7):1221–1232.e7.
62. Collomb E, Yang Y, Foriel S, Cadau S, Pearton DJ, Dhouailly D. The corneal epithelium and lens develop independently from a common pool of precursors. *Dev Dyn*. 2013;242(5):401–413.
63. Sullivan DA, Hann LE. Hormonal influence on the secretory immune system of the eye: Endocrine impact on the lacrimal gland accumulation and secretion of IgA and IgG. *J Steroid Biochem*. 1989;34(1–6):253–262.
64. Richards SM, Jensen RV, Liu M, et al. Influence of sex on gene expression in the mouse lacrimal gland. *Exp Eye Res*. 2006;82(1):13–23.
65. Hat K, Planinić A, Ježek D, Kaštelan S. Expression of androgen and estrogen receptors in the human lacrimal gland. *Int J Mol Sci*. 2023;24(6):5609.
66. Imada T, Nakamura S, Hisamura R, et al. Serotonin hormonally regulates lacrimal gland secretory function via the serotonin type 3a receptor. *Sci Rep*. 2017;7(1):6965.
67. Cvekl A, Yang Y, Chauhan BK, Cveklova K. Regulation of gene expression by Pax6 in ocular cells: a case of tissue-preferred expression of crystallins in lens. *Int J Dev Biol*. 2004;48(8-9):829–844.
68. Kitazawa K, Hikichi T, Nakamura T, Sotozono C, Kinoshita S, Masui S. PAX6 regulates human corneal epithelium cell identity. *Exp Eye Res*. 2017;154:30–38.
69. Zhu L, Chen C, Wu S, et al. PAX6-WNK2 axis governs corneal epithelial homeostasis. *Invest Ophthalmol Vis Sci*. 2024;65(12):40.
70. Koppaka V, Chen Y, Mehta G, et al. ALDH3A1 plays a functional role in maintenance of corneal epithelial homeostasis. *PLoS One*. 2016;11(1):e0146433.
71. Pappa A, Brown D, Koutalos Y, DeGregori J, White C, Vasiliou V. Human aldehyde dehydrogenase 3A1 inhibits proliferation and promotes survival of human corneal epithelial cells. *J Biol Chem*. 2005;280(30):27998–28006.
72. Voulgaridou GP, Theologidis V, Venetikidou M, et al. Investigating the functional roles of aldehyde dehydrogenase 3A1 in human corneal epithelial cells. *Int J Mol Sci*. 2023;24(6):5845.
73. Li Z, Stachon T, Zimmermann J, et al. Expression of PAX6 and keratocyte-characteristic markers in human limbal stromal cells of congenital aniridia and healthy subjects, in vitro. *Curr Eye Res*. 2025;50(4):362–372.
74. Simpson TI, Pratt T, Mason JO, Price DJ. Normal ventral telencephalic expression of Pax6 is required for normal development of thalamocortical axons in embryonic mice. *Neural Dev*. 2009;4(1):19.
75. Schwenk F, Baron U, Rajewsky K. A *cre* -transgenic mouse strain for the ubiquitous deletion of *loxP* -flanked gene segments including deletion in germ cells. *Nucl Acids Res*. 1995;23(24):5080–5081.
76. Robinson DO, Howarth RJ, Williamson KA, van Heyningen V, Beal SJ, Crolla JA. Genetic analysis of chromosome 11p13 and the *PAX6* gene in a series of 125 cases referred with aniridia. *Am J Med Genet A*. 2008;146A(5):558–569.
77. Latta L, Figueiredo FC, Ashery-Padan R, et al. Pathophysiology of aniridia-associated keratopathy: developmental aspects and unanswered questions. *Ocul Surf*. 2021;22:245–266.

Investigative Ophthalmology & Visual Science